

Aggregate Model of District Heating Network for Integrated Energy Dispatch: A Physically Informed Data-Driven Approach

Shuai Lu, *Member, IEEE*, Zihang Gao, Yong Sun, Suhan Zhang, *Member, IEEE*, Baoju Li, Chengliang Hao, Yijun Xu, *Senior Member, IEEE*, Wei Gu, *Senior Member, IEEE*

Abstract—The district heating network (DHN) is essential in enhancing the operational flexibility of integrated energy systems (IES). Yet, it is hard to obtain an accurate and concise DHN model for the operation owing to complicated network features and imperfect measurement. Considering this, this paper proposes a physically informed data-driven aggregate model (AGM) for DHN, providing a concise description of the source-load relationship of DHN without exposing network details. First, we derive the analytical relationship between the state variables of the source and load nodes of DHN, offering a physical fundament for the AGM. Second, we propose a physics-informed estimator for AGM that is robust to low-quality measurement, in which the physical constraints associated with the parameter normalization and sparsity are embedded to improve the accuracy and robustness. Finally, we propose a physics-enhanced algorithm to solve the nonlinear estimator with non-closed constraints efficiently. Simulation results verify the effectiveness of the proposed method.

Index Terms—Aggregate model, district heating network, integrated energy systems, physics-informed data-driven method.

I. NOMENCLATURE

A. Abbreviations

DHN	District heating network
AGM	Aggregate model
IES	Integrated energy systems
STM	Supply temperature mapping
RTM	Return temperature mapping
LSE	Least squares estimator
HME	Huber M-estimator

B. Sets

Φ_n, Φ_p	Index set of nodes/pipes in DHN
Φ_{ln}, Φ_{sn}	Index set of load/source nodes in DHN
Φ_{p+}^k, Φ_{p-}^k	Index set of pipelines flowing into/flowing out of node k
$\Phi_p^{k,v}$	Index set of pipes on the path between node k and node v
$\Delta^{k,v}$	Set of delay parameters from node k to node v

C. Parameters and Variables

Δt	Time length of interval (s)
A_p^j	Cross-section area of pipeline j (m ²)
L_p^j	Length of pipeline j (m)
λ_p^j	Heat loss coefficient of pipeline j (kW/(m·°C))
ρ_w	Heat medium density in DHN (kg/m ³)

$\gamma_p^j, R_p^j, \alpha_p^j, \eta_p^j$	Parameters of the node method model
c_w	Specific heat capacity of water (kJ/(kg·°C))
m_p^j	Mass flow rate of pipeline j (kg/s)
m_{src}^k, m_l^k	Mass flow rate of heat source/load at node k of DHN (kg/s)
$m_{src}^{k,v}$	Equivalent mass flow rate of the supply water from source node k to load node v
$m_l^{k,v}$	Equivalent mass flow rate of the return water from load node v to source node k
τ_{amb}	Ambient temperature of DHN (°C)
$\tau_{s,src}^{k,t}, \tau_{r,src}^{k,t}$	Supply/return temperature of heat source at node k at period t (°C)
$\tau_{s,l}^{k,t}, \tau_{r,l}^{k,t}$	Supply/return temperature of heat load at node k (°C)
$\tau_{s,n}^{k,t}, \tau_{r,n}^{k,t}$	Supply/return temperature at node k (°C)
$\tau_{s,in}^{j,t}, \tau_{s,out}^{j,t}$	Inlet/outlet temperature of supply pipeline j (°C)
$\tau_{r,in}^{j,t}, \tau_{r,out}^{j,t}$	Inflow/outflow temperature of return pipeline j (°C)
$\tau_{s,src}^t, \tau_{r,src}^t$	Supply/return temperature vector of source
$\tau_{s,l}^t, \tau_{r,l}^t$	Supply/return temperature vector of load
Γ	Maximum delay of DHN
N_s, N_l	Number of source/load nodes in DHN
$N_p^{k,v}$	Number of pipelines on the shortest path between node k and node v
$a_s^{k,v,i}, b_s^{k,v}$	Aggregate parameters between node k and node v in supply network of AGM
$a_r^{k,v,i}, b_r^{k,v}$	Aggregate parameters between node k and node v in return network of AGM
$\gamma_{agg}^{k,v}$	Transmission delay from node k to node v
$\xi_s^{k,v}$	Proportion of water mass from source node k to that flows into load node v
$\xi_r^{k,v}$	Proportion of water mass from load node v to that flows into source node k
$\tilde{a}_{s/r}^{k,v,i}, \tilde{b}_{s/r}^{k,v}$	Model parameters of the AGM
$\tilde{a}_s^k, \tilde{a}_r^v$	Parameter matrix of the AGM
M, M_{trc}	Original/truncated horizon of regression model
$\mathbf{r}_s^v, \mathbf{r}_r^k$	Residual vector of node k/v in supply/return network
$r_s^{v,t}, r_r^{k,t}$	Residual at time t of node k/v in supply/return network
$\hat{\sigma}_s^v$	The scale estimate of residuals of the supply temperature at load node v
κ	Tuning constant of Huber M-estimator

1. INTRODUCTION

Today's increasing energy consumption and environmental degradation have generated a huge demand for improving energy efficiency and reducing carbon emissions. Integrated energy systems (IES), which combine various energy carriers and networks, have received much attention [1]. The district heating network (DHN) plays a vital role in IES because it can provide considerable flexibility for the system operation [2, 3]. Specifically, as an energy carrier, the heat medium in the DHN has excellent energy storage capacity, i.e., thermal inertia [4, 5]. In practice, the DHN and power system are usually managed by different operators, making their coordination difficult. On the one hand, an accurate DHN model that can describe the network characteristics is necessary to exploit the thermal inertia while ensuring heating quality. On the other hand, a cumbersome DHN model not only has the risk of exposing sensitive information about district heating systems to power system operators but also brings in excess computational burden for the operation. Therefore, it has been recognized that an accurate and concise DHN model is essential for the operation of IES.

Typically, the modeling of DHN can be divided into two categories, i.e., the physics-based methods and the data-driven methods. The former directly employs physical laws to construct the DHN models [6, 7]. Typical examples include the element method [8], characteristic method [9], and node method [10]. Both the element method and the characteristic method divide the pipeline into many discrete "units" or "nodes", which need to be calculated in each calculation step, requiring a large amount of calculation. Compared to the above two models, the node method model has a faster computing speed [11]. Within it, the development of a pipeline model has two steps: first, the transmission delay is tracked by calculating the time of heat medium flowing through the pipeline; then, the heat loss in the transmission process is considered [12]. The accuracy of the node method has been verified in multiple real-world DHNs [13, 14]. The same philosophy among these methods emphasizes the detailed modeling of each pipeline. Such a model is usually unsuitable for the optimization problem of IES, such as optimal planning and economic dispatch. More specifically, these models introduce many equations and variables for pipelines, resulting in a large-scale optimization problem that is hard to solve. Besides, the power system and district heating system are often owned by different entities, meaning that the above models will expose the detailed information of DHN to others and thus cause privacy issues.

Facing the above challenges, more research has paid attention to the equivalent modeling techniques, which are much simpler yet effective. Some early work tried simplifying the DHN model to reduce computational burden by aggregating the pipelines. Larsen *et al.* [15, 16] first proposed a DHN aggregate method known as "the Danish method". It reduces the DHN to an equivalent simpler network of pipe segments based on some over-bold assumptions, such as constant overall heat load. Bøhm *et al.* [17] further tested the model performance under different aggregate depths based on "the Danish method" and "the German method" [18]. However, these methods have several shortcomings. First, the assumptions (e.g., constant overall heat load) in these methods usually cannot always hold, causing significant errors in the highly aggregated model [17]. Second,

"the Danish method" requires detailed parameters, such as pipeline length and diameter. This inevitably places exceptionally high demands on the integrity and accuracy of the internal parameters.

Unlike the physics-driven methods that have been extensively explored, the related works for the data-driven ones are just a few, in which the time series method and neural networks are popular ones [19]. La Bella *et al.* [20] proposed a piece-wise Auto Regressive eXogenous back-box method for DHN modeling. This method can learn from the artificially generated data to build a model approximating the original nonlinear model. Although the models approximated from real-world measurements are more convincing, the data-driven DHN model suffers from several problems. First, the measurement in practice is often scarce and incomplete. This is especially true for the inner pipelines and nodes of the DHN, which are usually not equipped with measurement units at all. Here, in most situations, only the operational data of source and load nodes are available. Second, the accuracy of data-driven methods depends on the quantity and quality of the data [19, 21].

To address them, a few recent works have noticed the above problems and attempted to develop the equivalent DHN model from a network perspective to avoid using the inner state data of DHN. Zheng *et al.* [22] first derived an equivalent matrix model for DHN that directly reveals the relationship between the boundary control and inner state variables. However, this model still needs the complete measurement to estimate the parameters since the inner states are kept. Zhang *et al.* [23] further derived the source-load function of DHN as the linear combination of the initial and boundary conditions based on the partial differential model of pipelines. Albeit simple, this method relies on detailed parameters to calculate the combination coefficients while the parameters estimation problem is ignored.

In summary, it is still an unresolved issue to develop a practical and interpretable DHN model in a data-driven manner for the optimization problem of IES that features low computational complexity and non-exposure of the inner states of network. The potential challenges are multifold. First, it needs to be further explored at the physics level regarding the accuracy of the DHN model without the internal network states. Second, although the DHN with some specific control strategies (e.g., the constant-flow strategy) is typically a linear system, its inverse problem, i.e., the parameter estimation, will be much more complicated because of the incomplete measurement. Also, the potential problem of low-quality measurement in engineering will bias the estimation results.

To address the abovementioned problems, we propose a physically informed data-driven aggregate model (AGM) for DHN by combining the advantages of physics and operational data. The proposed AGM has a concise mathematical form and clear physical connotation, yielding a cost-effective DHN model for the optimization problem of IES. In particular, the physical characteristics of the DHN are well exploited in the estimation of the AGM to improve the model accuracy and reduce the computational burden. Case studies based on different scales of DHN verify the effectiveness of the proposed method. We further demonstrate the practicality of the AGM through the case studies in the economic dispatch of IES.

The main contributions are summarized as follows:

- (1) We derive the AGM of DHN that directly reveals the

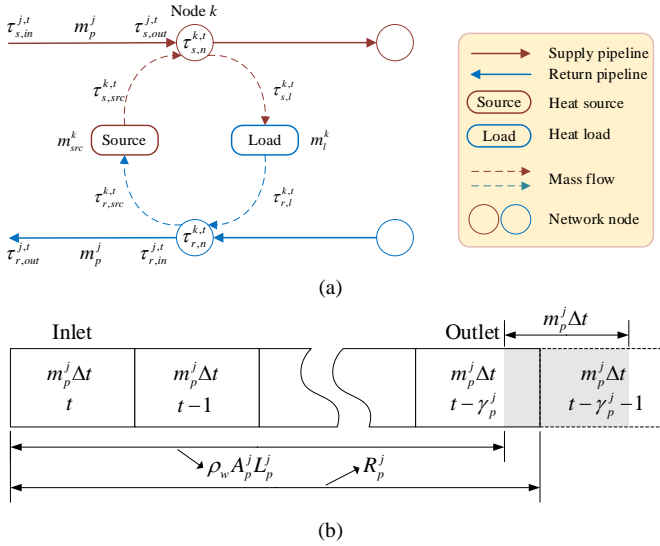


Fig. 1 The basic elements of DHN: (a) The structure of the DHN; (b) The pipeline model based on node method.

input-output relationship of network. The AGM consists of the supply temperature mapping (STM) of load nodes and the return temperature mapping (RTM) of source nodes, simplifying the DHN into a source-load mapping network by eliminating inner nodes.

- (2) We propose a physics-enhanced method for the parameter estimation of AGM. The accuracy and robustness of the estimator are improved by integrating the parameter constraints derived from the physical properties of DHN, including the parameter normalization and sparsity.
- (3) The proposed estimator is a non-closed nonlinear optimization model due to the presence of a delay parameter in the variable index, making off-the-shelf solvers ineffective. To solve it, we propose the delay parameter enumeration-based iterative reweighted least squares (IRLS) algorithm, in which a successive estimation strategy of STM and RTM are introduced to avoid the combinatorial explosion problem.

The remainder of this paper is organized as follows. Section II introduces the AGM; Section III proposes the physics-informed robust parameter estimator for AGM and the corresponding physics-enhanced solution algorithm; Section IV verifies the effectiveness of the proposed method by numerical tests; and Section V concludes this paper.

II. AGGREGATE MODEL OF DHN

In this section, we will first briefly introduce the physical model of DHN. Second, we will give the concept of the AGM. The detailed derivation of the AGM is then presented.

A. Physical Model of DHN

This paper focuses on the DHN that operates under the widely-used constant flow and variable temperature control strategy [24, 25]. The basic elements of DHN are illustrated in Fig. 1 (a). The DHN model consists of the heat transmission equation of pipelines, the energy balance equations of nodes, and the temperature fusion equations of nodes [25]. We use the node method [10] to model the heat transmission in the pipeline, as illustrated in Fig. 1 (b). Based on the node method, the outlet

temperature of the pipeline considering the transmission delay and heat loss can be calculated as

$$\tau_{x,out}^{j,t} = (1 - \eta_p^j) \left((1 - \alpha_p^j) \tau_{x,in}^{j,t - \gamma_p^j - 1} + \alpha_p^j \tau_{x,in}^{j,t - \gamma_p^j} \right) + \eta_p^j \tau_{amb}^j \quad (1a)$$

$$\forall j \in \Phi_p, x \in \{s, r\}$$

The parameters α_p^j , η_p^j , and γ_p^j can be calculated as follows

$$\begin{cases} \gamma_p^j = \lceil \rho_w A_p^j L_p^j / (m_p^j \Delta t) \rceil - 1 \\ R_p^j = (\gamma_p^j + 1) m_p^j \Delta t \\ \alpha_p^j = (R_p^j - \rho_w A_p^j L_p^j) / (m_p^j \Delta t) \\ \eta_p^j = 1 - \exp \left(- \frac{\lambda_p^j \Delta t}{\rho_w A_p^j c_w} (\gamma_p^j + 3/2 - \alpha_p^j) \right) \end{cases}, \quad (1b)$$

wherein $\lceil \cdot \rceil$ is the ceiling function.

The energy balance equations of nodes are as

$$\begin{cases} m_{src}^k \tau_{s,src}^{k,t} + \sum_{j \in \Phi_{p+}^k} m_p^j \tau_{s,out}^{j,t} = (m_{src}^k + \sum_{j \in \Phi_{p+}^k} m_p^j) \tau_{s,n}^{k,t} \\ m_l^k \tau_{r,l}^{k,t} + \sum_{j \in \Phi_{p-}^k} m_p^j \tau_{r,out}^{j,t} = (m_l^k + \sum_{j \in \Phi_{p-}^k} m_p^j) \tau_{r,n}^{k,t} \end{cases} \quad \forall k \in \Phi_n. \quad (1c)$$

The temperature fusion equations of nodes are as

$$\begin{cases} \tau_{s,in}^{j,t} |_{\forall j \in \Phi_{p-}^k} = \tau_{s,n}^{k,t}, \quad \tau_{r,in}^{j,t} |_{\forall j \in \Phi_{p+}^k} = \tau_{r,n}^{k,t} \\ \tau_{r,src}^{k,t} = \tau_{r,n}^{k,t}, \quad \tau_{s,l}^{k,t} = \tau_{s,n}^{k,t} \end{cases} \quad \forall k \in \Phi_n. \quad (1d)$$

Remark 1. In real-world applications, it is impractical to model DHN based on equations (1a)-(1d). First, there are usually no measurement units for the pipelines and nodes inner the DHN, making the inner operational data unavailable. Second, equations (1a)-(1d) will expose detailed information about the DHN, bringing serious privacy concerns [26]. Moreover, they have many variables and equations, increasing the computational cost.

B. Concept of Aggregate Model

The concept of the AGM is shown in Fig. 2, which includes the supply network and the return network. In the supply network, the supply temperature of load nodes can be directly represented by the supply temperature of the source nodes. In the return network, the return temperature of the source nodes can be directly represented by the return temperature of the load nodes. The mathematical model includes the STM and RTM, as

$$\text{STM:} \quad \tau_{s,l}^t = S(\tau_{s,src}^t), \quad (2a)$$

$$\text{RTM:} \quad \tau_{r,src}^t = R(\tau_{r,l}^t), \quad (2b)$$

wherein S and R are vector-valued functions, and $S: \mathbb{R}^{\Gamma \times N_s} \rightarrow \mathbb{R}^{1 \times N_l}$, $R: \mathbb{R}^{\Gamma \times N_l} \rightarrow \mathbb{R}^{1 \times N_s}$, which are defined as

$$\tau_{s,src}^t = \begin{bmatrix} \tau_{s,src}^{1,t-\Gamma} & \dots & \tau_{s,src}^{N_s,t-\Gamma} \\ \vdots & \ddots & \vdots \\ \tau_{s,src}^{1,t} & \dots & \tau_{s,src}^{N_s,t} \end{bmatrix}, \quad \tau_{r,l}^t = \begin{bmatrix} \tau_{r,l}^{1,t-\Gamma} & \dots & \tau_{r,l}^{N_l,t-\Gamma} \\ \vdots & \ddots & \vdots \\ \tau_{r,l}^{1,t} & \dots & \tau_{r,l}^{N_l,t} \end{bmatrix}, \quad (2c)$$

$$\tau_{s,l}^t = [\tau_{s,l}^{1,t} \dots \tau_{s,l}^{N_l,t}]^T, \quad \tau_{r,src}^t = [\tau_{r,src}^{1,t} \dots \tau_{r,src}^{N_s,t}]^T. \quad (2d)$$

In practical engineering, we can use the measurement of the temperature at the source and load nodes to estimate the

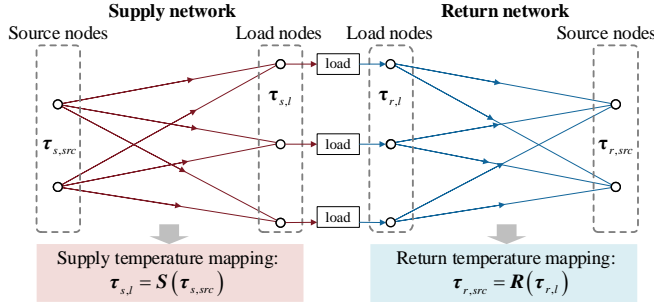


Fig. 2 Concept of the AGM of DHN.

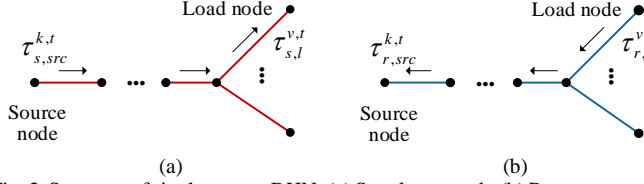


Fig. 3 Structure of single-source DHN: (a) Supply network; (b) Return network.

function $S(\cdot)$ and $R(\cdot)$. The detailed derivation of the STM and RTM is introduced in the following.

C. Formation of AGM

First, we derive the AGM for single-source DHN, which is first introduced in [24]. Fig. 3 (a) gives a basic structure in a single-source radial DHN. Based on the recursion of the equation (1a), the supply temperature of the load node v can be calculated as

$$\tau_{s,l}^{v,t} = \sum_{i=0}^{N_p^{k,v}} \left(a_s^{k,v,i} \tau_{s,src}^{k,t-\gamma_{agg}^{k,v}-i} \right) + b_s^{k,v} \tau_{amb} \quad \forall v \in \Phi_{ln}, \quad (3a)$$

wherein the aggregate parameter $a_s^{k,v,i}$, $b_s^{k,v}$, and $\gamma_{agg}^{k,v}$ are calculated as

$$a_s^{k,v,i} = \begin{cases} a_s^{v-1,v,0} a_s^{k,v-1,0}, & i=0 \\ \sum_{n=0}^1 a_s^{v-1,v,n} a_s^{k,v-1,i-n}, & 1 \leq i \leq v-k-1, \\ a_s^{v-1,v,1} a_s^{k,v-1,v-k-1}, & i=v-k \end{cases} \quad (3b)$$

$$b_s^{k,v} = 1 - \prod_{j \in \Phi_p^{k,v}} (1 - \eta_p^j), \quad (3c)$$

$$\gamma_{agg}^{k,v} = \sum_{j \in \Phi_p^{k,v}} \gamma_p^j, \quad (3d)$$

wherein the parameters $a_s^{j-1,j,0}$ and $a_s^{j-1,j,1}$ are defined as

$$\begin{cases} a_s^{j-1,j,0} = (1 - \eta_p^j) \alpha_p^j \\ a_s^{j-1,j,1} = (1 - \eta_p^j) (1 - \alpha_p^j) \end{cases} \quad j \in \Phi_p^{k,v}. \quad (3e)$$

The detailed derivation of (3a)-(3e) is given in [30].

Since the DHN under the constant flow and variable temperature control strategy is a linear time-invariant system (taking $\tau_{s,src}^{k,t}$ and τ_{amb} as the input and $\tau_{s,l}^{v,t}$ as the output), the superposition theorem holds for it. Therefore, the return temperature of the source node k can be easily calculated as

$$\tau_{r,src}^{k,t} = \sum_{v \in \Phi_{ln}} \xi_r^{k,v} \sum_{i=0}^{N_p^{k,v}} \left(a_r^{k,v,i} \tau_{r,l}^{v,t-\gamma_{agg}^{k,v}-i} + b_r^{k,v} \tau_{amb} \right), \quad (3f)$$

wherein the parameter $a_r^{k,v,i}$, $b_r^{k,v}$, and $\xi_r^{k,v}$ are defined as

$$a_r^{k,v,i} = a_s^{k,v,i}, b_r^{k,v} = b_s^{k,v}, \xi_r^{k,v} = \frac{m_l^{k,v}}{\sum_{i \in \Phi_{ln}} m_l^{k,i}}. \quad (3g)$$

Based on the above, the AGM for the multi-source DHN can be easily derived based on the superposition theorem, as

$$\tau_{s,l}^{v,t} = \sum_{k \in \Phi_{sn}} \xi_s^{k,v} \left(\sum_{i=0}^{N_p^{k,v}} a_s^{k,v,i} \tau_{s,src}^{k,t-\gamma_{agg}^{k,v}-i} + b_s^{k,v} \tau_{amb} \right) \quad \forall v \in \Phi_{ln}, \quad (4a)$$

$$\tau_{r,src}^{k,t} = \sum_{v \in \Phi_{ln}} \xi_r^{k,v} \left(\sum_{i=0}^{N_p^{k,v}} a_r^{k,v,i} \tau_{r,l}^{v,t-\gamma_{agg}^{k,v}-i} + b_r^{k,v} \tau_{amb} \right) \quad \forall k \in \Phi_{sn}. \quad (4b)$$

In (4a), the coefficient $\xi_s^{k,v}$ is a constant representing the proportion of the water mass from the source node k (i.e., $m_l^{k,v}$) to that flow into the load node v (i.e., $\sum_{k \in \Phi_{sn}} m_l^{k,v}$); and the coefficient $\xi_r^{k,v}$ is a constant representing the proportion of the water mass from the load node v (i.e., $m_{src}^{k,v}$) to that flow into the source node k (i.e., $\sum_{v \in \Phi_{ln}} m_{src}^{k,v}$). The expressions of them are as

$$\xi_s^{k,v} = \frac{m_l^{k,v}}{\sum_{k \in \Phi_{sn}} m_l^{k,v}}, \xi_r^{k,v} = \frac{m_{src}^{k,v}}{\sum_{k \in \Phi_{ln}} m_{src}^{k,v}}. \quad (4c)$$

Because the water mass from multiple sources will mix before flowing into the load nodes, the proportions of the water mass from the source k in $m_l^{k,v}$ are agnostic, leaving $\xi_s^{k,v}$ and $\xi_r^{k,v}$ without explicit expressions.

Equations (4a)-(4b) give the expressions of the STM and RTM defined in (2a) and (2b), which can be recast as

$$\tau_{s,l}^{v,t} = S^v(\tau_{s,src}^t) = \mathbf{1}^T (\tilde{\mathbf{a}}_s^v \circ \tau_{s,src}^t) \mathbf{1} + \tilde{\mathbf{b}}_s^v \tau_{amb} \quad \forall v \in \Phi_{ln}, \quad (5a)$$

$$\tau_{r,src}^{k,t} = R^k(\tau_{r,l}^t) = \mathbf{1}^T (\tilde{\mathbf{a}}_r^k \circ \tau_{r,l}^t) \mathbf{1} + \tilde{\mathbf{b}}_r^k \tau_{amb} \quad \forall k \in \Phi_{sn}, \quad (5b)$$

wherein \circ is Hadamard product, $S^v(\cdot)$ and $R^k(\cdot)$ are the v th and k th element in $S(\cdot)$ and $R(\cdot)$, respectively, and the parameters $\tilde{\mathbf{a}}_s^v$, $\tilde{\mathbf{a}}_r^k$, $\tilde{\mathbf{b}}_s^v$, and $\tilde{\mathbf{b}}_r^k$ are defined as

$$\tilde{\mathbf{a}}_s^v = \begin{bmatrix} \tilde{a}_s^{1,v,\Gamma} & \dots & \tilde{a}_s^{N_s,v,\Gamma} \\ \vdots & \ddots & \vdots \\ \tilde{a}_s^{1,v,0} & \dots & \tilde{a}_s^{N_s,v,0} \end{bmatrix}, \tilde{\mathbf{a}}_r^k = \begin{bmatrix} \tilde{a}_r^{k,1,\Gamma} & \dots & \tilde{a}_r^{k,1,\Gamma} \\ \vdots & \ddots & \vdots \\ \tilde{a}_r^{k,1,0} & \dots & \tilde{a}_r^{k,N_l,0} \end{bmatrix}, \quad (5c)$$

$$\tilde{\mathbf{b}}_s^v = \sum_{k \in \Phi_{sn}} \xi_s^{k,v} b_s^{k,v}, \tilde{\mathbf{b}}_r^k = \sum_{v \in \Phi_{ln}} \xi_r^{k,v} b_r^{k,v}, \quad (5d)$$

wherein Γ , $\tilde{a}_s^{k,v,i}$, and $\tilde{a}_r^{k,v,i}$ are defined as

$$\Gamma = \max_{k \in \Phi_{sn}, v \in \Phi_{ln}} (\gamma_{agg}^{k,v} + N_p^{k,v}), \quad (5e)$$

$$\begin{aligned} \tilde{a}_s^{k,v,i} &= \begin{cases} \xi_s^{k,v} a_s^{k,v,i-\gamma_{agg}^{k,v}} & 0 \leq i - \gamma_{agg}^{k,v} \leq N_p^{k,v} \\ 0 & \text{others} \end{cases} \\ \tilde{a}_r^{k,v,i} &= \begin{cases} \xi_r^{k,v} a_r^{k,v,i-\gamma_{agg}^{k,v}} & 0 \leq i - \gamma_{agg}^{k,v} \leq N_p^{k,v} \\ 0 & \text{others} \end{cases} \end{aligned} \quad (5f)$$

The definition in (5f) can be directly derived from (4a)-(4b). Taking (4a) as an example, for the temperature of the source node k , the coefficients of $\tau_{s,src}^{k,t-\gamma_{agg}^{k,v}-i}$, i.e., $a_s^{k,v,i}$, is nonzero only when $i = 0, \dots, N_p^{k,v}$.

For the AGM (5a)-(5b), once we get the measurement $\tau_{s,src}^t$, $\tau_{r,l}^t$, $\tau_{s,l}^{v,t}$, $\tau_{r,src}^{k,t}$, and τ_{amb} , the model parameters including $\tilde{\mathbf{a}}_s^v$, $\tilde{\mathbf{a}}_r^k$, $\tilde{\mathbf{b}}_s^v$, and $\tilde{\mathbf{b}}_r^k$ can be estimated.

Remark 2. Although the STM and RTM are linear systems, as shown in (5a) and (5b), the inverse problem, i.e., the parameter estimation, is much more difficult because of the unknown structure of $\tilde{\mathbf{a}}_s^v$ and $\tilde{\mathbf{a}}_r^k$. The reason is that the unknown delay parameters of the DHN ($\gamma_{agg}^{k,v}$) and the number of pipelines between sources and loads ($N_p^{k,v}$) introduce the parameters to be estimated into the time index, as shown in (5f). Essentially, this is caused by the incomplete measurement of the DHN, i.e., the mass flow rates of pipelines (and the corresponding pipeline lengths and network topology) are not included in the measurement in engineering.

III. PHYSICS-INFORMED ROBUST PARAMETER ESTIMATION OF AGM

In this section, we develop the robust parameter estimation model for AGM. Then, the delay parameter enumeration-based IRLS algorithm is proposed to solve this model efficiently.

A. Physics-Informed Robust Parameter Estimator

1) Robust estimation model

The models defined in (5a)-(5f) show that $\tau_{s,l}^{v,t}$ is an affine function of $\tau_{s,src}^{k,t-\Gamma}$, $\tau_{s,src}^{k,t-\Gamma+1}$, ..., $\tau_{s,src}^{k,t}$, $k \in \Phi_{sn}$, and $\tau_{r,src}^{k,t}$ is an affine function of $\tau_{r,l}^{v,t-\Gamma}$, $\tau_{r,l}^{v,t-\Gamma+1}$, ..., $\tau_{r,l}^{v,t}$, $v \in \Phi_{ln}$. Therefore, we can model $\tau_{s,l}^{v,t}$ as a M -horizon linear regression model of $\tau_{s,src}^{k,t}$, $k \in \Phi_{sn}$ and $\tau_{r,src}^{k,t}$ as a M -horizon linear regression model of $\tau_{r,l}^{v,t}$, $v \in \Phi_{ln}$, respectively, wherein M is defined as

$$M = \Gamma - \gamma_{agg}^{k,v}. \quad (6)$$

Based on this, the least squares estimator (LSE) can be used to obtain the parameters of the AGM, as

$$\forall v \in \Phi_{ln} : \min_{\tilde{\mathbf{a}}_s^v, \tilde{\mathbf{b}}_s^v} J_s^v(\tilde{\mathbf{a}}_s^v, \tilde{\mathbf{b}}_s^v) = \frac{1}{2} (\mathbf{r}_s^v)^T \mathbf{r}_s^v, \quad (7a)$$

$$\forall k \in \Phi_{sn} : \min_{\tilde{\mathbf{a}}_r^k, \tilde{\mathbf{b}}_r^k} J_r^k(\tilde{\mathbf{a}}_r^k, \tilde{\mathbf{b}}_r^k) = \frac{1}{2} (\mathbf{r}_r^k)^T \mathbf{r}_r^k. \quad (7b)$$

wherein the residual vectors \mathbf{r}_s^v and \mathbf{r}_r^k are defined as

$$\mathbf{r}_s^v = \begin{bmatrix} r_{s,l}^{v,1}, \dots, r_{s,l}^{v,T} \end{bmatrix}^T = \begin{bmatrix} \tau_{s,l}^{v,1} - S^v(\tau_{s,src}^1), \dots, \tau_{s,l}^{v,T} - S^v(\tau_{s,src}^T) \end{bmatrix}^T, \quad (7c)$$

$$\mathbf{r}_r^k = \begin{bmatrix} r_{r,l}^{k,1}, \dots, r_{r,l}^{k,T} \end{bmatrix}^T = \begin{bmatrix} \tau_{r,l}^{k,1} - R^k(\tau_{r,l}^1), \dots, \tau_{r,l}^{k,T} - R^k(\tau_{r,l}^T) \end{bmatrix}^T. \quad (7d)$$

In practical engineering, the quality of the measurement of DHN cannot be guaranteed owing to many factors, such as environmental noise and poor communication quality. Hence, we use the Huber M-estimator (HME) to improve the robustness against the anomalies and outliers in the measurement. In the following, we only focus on (7a) for conciseness, but the method also applies to (7b).

Based on the HME, the LSE in (7a) is replaced by

$$\forall v \in \Phi_{ln} : \min_{\tilde{\mathbf{a}}_s^v, \tilde{\mathbf{b}}_s^v} J_s^v(\tilde{\mathbf{a}}_s^v, \tilde{\mathbf{b}}_s^v) = \sum_{t \in T} J_s^{v,t}(\tilde{\mathbf{a}}_s^v, \tilde{\mathbf{b}}_s^v), \quad (8a)$$

wherein $J_s^{v,t}(\mathbf{a}_s^v, \mathbf{b}_s^v)$ is the Huber loss, defined as

$$J_s^{v,t}(\tilde{\mathbf{a}}_s^v, \tilde{\mathbf{b}}_s^v) = \begin{cases} \frac{1}{2} (\mathbf{r}_s^{v,t} / \hat{\sigma}_s^v)^2 & |\mathbf{r}_s^{v,t} / \hat{\sigma}_s^v| \leq \kappa \\ \kappa |\mathbf{r}_s^{v,t} / \hat{\sigma}_s^v| - \frac{1}{2} \kappa^2 & |\mathbf{r}_s^{v,t} / \hat{\sigma}_s^v| > \kappa \end{cases}, \quad (8b)$$

wherein $\hat{\sigma}_s^v$ is the scale estimate of residuals, and κ is a tuning constant (1.345 in this paper).

The scale estimate $\hat{\sigma}_s^v$ in (8b) is chosen as the median absolute deviation of the residuals, as

$$\hat{\sigma}_s^v = 1.4826 \cdot \text{med} \{ |\hat{r}_s^{v,t}| : \hat{r}_s^{v,t} \neq 0 \}_{t \in T}. \quad (8c)$$

2) Physics-informed estimator enhancement

We notice that the physics below the AGM endows the parameters $\tilde{\mathbf{a}}_s^v$ and $\tilde{\mathbf{a}}_r^k$ with a special structure, including the normalization and sparsity.

First, as indicated by the expressions of $\tilde{\mathbf{a}}_s^{k,v,i}$, $\tilde{\mathbf{a}}_r^{k,v,i}$, $\tilde{\mathbf{b}}_s^v$, $\tilde{\mathbf{b}}_r^k$ in (5d), (5f) and the definitions (3b), (3c), (3g), (4c), we have the normalization constraints, as

$$\mathbf{1}^T \tilde{\mathbf{a}}_s^v \mathbf{1} + \tilde{\mathbf{b}}_s^v = 1, \quad \forall v \in \Phi_{sn}, \quad \mathbf{1}^T \tilde{\mathbf{a}}_r^k \mathbf{1} + \tilde{\mathbf{b}}_r^k = 1, \quad \forall k \in \Phi_{ln}. \quad (9a)$$

Intuitively, the normalization constraints (9a) originate from the energy conservation law of the network. The detailed derivation of (9a) is given in [30].

Second, the equations in (5c) and (5f) indicate that the matrices $\tilde{\mathbf{a}}_s^v$ and $\tilde{\mathbf{a}}_r^k$ should be sparse. These two features should be also embedded into the estimator in the form of constraints, as

$$(\tilde{\mathbf{a}}_s^v, \tilde{\mathbf{b}}_s^v) \in \Lambda_s^v \quad \forall v \in \Phi_{sn}, \quad (\tilde{\mathbf{a}}_r^k, \tilde{\mathbf{b}}_r^k) \in \Lambda_r^k \quad \forall k \in \Phi_{ln}, \quad (9b)$$

wherein Λ_s^v and Λ_r^k include the equations (9a) and the sparse structural properties.

Now, we can get the expression of the STM (5a) by solving (8a) and (9b). However, the equations (5e) and (6) indicate that the horizon M will be very large if the scale of DHN is large, making the AGM tedious and not convenient for practical use. Fortunately, the equations (3b), (3e) and (3g) inspire a simplification method. Specifically, the equations (3b) indicate that the value of $\alpha_p^{k,v,i}$ approximates 0 when i approximates 0 or $k - v$ since $0 \leq \alpha_p^j \leq 1$ and $0 < 1 - \eta_p^j < 1$. Hence, we can use a truncated model with M_{trc} horizons ($M_{trc} \ll M$) to approximate the original model. This is equivalent to using a new $\tilde{\Lambda}_s^v$ (or $\tilde{\Lambda}_r^k$) with a sparser structure for $\tilde{\mathbf{a}}_s^v$ (or $\tilde{\mathbf{a}}_r^k$) to approximate Λ_s^v (or Λ_r^k). Hence, the constraints (9b) are replaced by

$$(\tilde{\mathbf{a}}_s^v, \tilde{\mathbf{b}}_s^v) \in \hat{\Lambda}_s^v \quad \forall v \in \Phi_{sn}, \quad (\tilde{\mathbf{a}}_r^k, \tilde{\mathbf{b}}_r^k) \in \hat{\Lambda}_r^k \quad \forall k \in \Phi_{ln}. \quad (10)$$

Finally, the HME for the STM of the AGM is formulated as

$$\forall v \in \Phi_{ln} : \min_{(\tilde{\mathbf{a}}_s^v, \tilde{\mathbf{b}}_s^v) \in \hat{\Lambda}_s^v} J_s^v(\tilde{\mathbf{a}}_s^v, \tilde{\mathbf{b}}_s^v) = \sum_{t \in T} J_s^{v,t}(\tilde{\mathbf{a}}_s^v, \tilde{\mathbf{b}}_s^v). \quad (11)$$

Remark 3. Since the estimator (11) integrates the physical properties of the DHN, including the normalization and sparsity constraints, its performance, including accuracy and robustness, will be enhanced. Theoretically, this is because the inherent structure of the AGM originating from the physical properties of DHN is enforced by the normalization constraints sparsity constraints and thus will not be destroyed by low-quality measurement. Numerical results will also verify this.

Algorithm 1. The IRLS method for the HME.

```

1: Initialize: set  $\kappa=1.345$ ,  $\text{Flag}=1$ ,  $i = 0$ , and tolerance  $\epsilon$ .
2: Calculate an initial estimate  $(\hat{\mathbf{a}}_s^v, \hat{\mathbf{b}}_s^v)_0$  by LSE, and calculate the
   residual  $(\mathbf{r}_s^v)_i$  by (7c) and scale  $(\hat{\sigma}_s^v)_i$  by (8c).
3: While Flag
4:   Update  $i = i + 1$ .
5:   For  $t = 1 : T$ 
6:     If  $|(r_s^{v,t})_{i-1}/(\hat{\sigma}_s^v)_{i-1}| \leq \kappa$ , set  $\omega_i^t = 1$ ;
7:     Else, set  $\omega_i^t = \kappa/|(r_s^{v,t})_{i-1}/(\hat{\sigma}_s^v)_{i-1}|$ .
8:   End
9:   Solve  $(\hat{\mathbf{a}}_s^v, \hat{\mathbf{b}}_s^v)_i = \text{argmin}_{(\tilde{\mathbf{a}}_s^v, \tilde{\mathbf{b}}_s^v) \in \tilde{\Lambda}_s^v} \sum_{t \in T} \frac{1}{2} \omega_i^t (r_s^{v,t}/(\hat{\sigma}_s^v)_i)^2$ .
10:  Calculate the residual  $(\mathbf{r}_s^v)_i$  by (7c) and scale  $(\hat{\sigma}_s^v)_i$  by (8c).
11:  If  $\|(\mathbf{r}_s^v)_i - (\mathbf{r}_s^v)_{i-1}\| \leq \epsilon$ 
12:    Set  $\text{Flag}=0$ .
13:  End
14: End While

```

B. Physics-Enhanced Solution Algorithm

Usually, the classical IRLS algorithm is efficient in solving the HME, as given in **Algorithm 1**. However, the IRLS method does not apply to (11) because of the presence of the structural constraint (10). As explained in **Remark 2**, this constraint results in the locations and numbers of the non-zeros in $\tilde{\mathbf{a}}_s^v$ are unknown. Such a structural feature cannot be described by a closed-form expression, making the models (11) a nonlinear optimization problem with non-closed constraints.

Note that although the value of Γ cannot be known in advance, it can be set to a large value bigger than the largest transmission delay of the DHN. This will make no difference except introducing more zeros in $\tilde{\mathbf{a}}_s^v$ and $\tilde{\mathbf{a}}_r^k$. Therefore, the fundamental difficulty is to keep the sparsity of $\tilde{\mathbf{a}}_s^v$ and $\tilde{\mathbf{a}}_r^k$. Specifically, the nonzeros in the k th column of $\tilde{\mathbf{a}}_s^v$ should be adjacent, and their number should be equal to M_{trc} .

Remark 4. Generally, we can introduce binary variables to provide explicit expressions for such structural constraints. However, the model (11) will turn into a large-scale mixed-integer nonlinear programming problem since the number of binary variables required for the structural description is large, making the model a computation-intensive problem, especially for large-scale networks. More seriously, the IRLS method will not be applicable because the convergence cannot be ensured after introducing binary variables.

Fortunately, the definition in (5f) indicates that for the load node v , after the horizon number M_{trc} is set, the nonzeros in the k th column of $\tilde{\mathbf{a}}_s^v$ can be determined as $\tilde{\mathbf{a}}_s^{k,v,\delta^{k,v}+M_{trc}}, \dots, \tilde{\mathbf{a}}_s^{k,v,\delta^{k,v}+1}, \tilde{\mathbf{a}}_s^{k,v,\delta^{k,v}}$ if the delay parameter $\delta^{k,v}$ is prescribed. In this situation, the STM estimator (11) and the corresponding RTM estimator turn to be a traditional HME. Inspired by this, we propose the delay parameter enumeration-based IRLS method for (11), as shown in **Algorithm 2**. The core of this method is to solve the estimator (11) under a set of prescribed delay parameters $\delta^{k,v}$, $k \in \Phi_{sn}$, $v \in \Phi_{ln}$ and then choose the one that has the smallest residuals as the estimated delay parameter. Assuming the set of the delay parameter $\delta^{k,v}$ to be selected is $\Delta^{k,v} = \{\delta_1^{k,v}, \delta_2^{k,v}, \dots\}$, the number of times the HME needs

Algorithm 2. Delay parameter enumeration based IRLS method for the estimation of AGM.

```

1: S0: Prescribe  $\Delta^{k,v}$ ,  $k \in \Phi_{sn}$ ,  $v \in \Phi_{ln}$ .
2: S1. Estimation of STM:
3: For  $v = 1 : |\Phi_{ln}|$ 
4:   Generate all the combinations of the elements in  $\Delta^{k,v}$ ,  $k \in \Phi_{sn}$ , denoted as the set  $\Xi_1, \Xi_2, \dots$ .
5:   For  $i = 1 : \prod_{k \in \Phi_{sn}} |\Delta^{k,v}|$ 
6:     Prescribe the structure of  $\mathbf{a}_s^v$  based on  $\Xi_i$ .
7:     Using the IRLS method to solve the estimator for the STM, (11), and denote the residual as  $J_s^v(\Xi_i)$ .
8:   End
9:   Set  $\Xi_{opt} = \text{argmin}_{\Xi_i} J_s^v(\Xi_i)$ .
10: End
11: S2. Estimation of RTM:
12: For  $k = 1 : |\Phi_{sn}|$ 
13:   Prescribe the structure of  $\mathbf{a}_r^k$  based on  $\Xi_{opt}$ .
14:   Using IRLS method to solve the estimator for the RTM.
15: End

```

to be solved for the STM and RTM, K_s and K_r , respectively, can be calculated as

$$K_s = |\Phi_{ln}| \prod_{k \in \Phi_{sn}} |\Delta^{k,v}|, \quad (12a)$$

$$K_r = |\Phi_{sn}| \prod_{v \in \Phi_{ln}} |\Delta^{k,v}|. \quad (12b)$$

Theoretically, to get the best estimation of $\delta^{k,v}$, we need to compare the residual sum of STM and RTM under each combination of $\delta^{k,v}$. However, we note that the value of K_r will be huge even for a small scale of DHN, resulting combinational explosion problem, while that of K_s is modest. For example, for a DHN with 2 source loads and 10 load nodes, assuming that the number of delay parameters to be selected is 5 for each pair (k, v) , $k \in \Phi_{sn}$, $v \in \Phi_{ln}$, then we have $K_s=250$, $K_r=19531250$. Usually, we have $K_s \ll K_r$. Therefore, we propose to solve the STM estimators to obtain the delay parameters $\delta^{k,v}$ firstly, and then transfer the values of $\delta^{k,v}$ to the RTM estimators. By this method, the times that the estimator needs to be solved are as

$$K_{sum} = K_s + |\Phi_{ln}|. \quad (13)$$

Obviously, the proposed method dramatically reduces the computation burden, especially for a large scale of DHN. For example, for a DHN with 2 source loads and 100 load nodes, if the number of delay parameters to be selected is 5 for each pair (k, v) , $k \in \Phi_{sn}$, $v \in \Phi_{ln}$, we have $K_s=2500$ and $K_{sum}=2600$, meaning we only need to solve the estimators 2600 times.

Remark 5. Note that in real-world engineering, the number of the sources in a DHN is usually small, about 1~4, far less than the number of load nodes. Besides, the delay parameters $\delta^{k,v}$ under fixed mass flow are constant, indicating we can use some methods to estimate their ranges. A practical way is to estimate based on historical results. If the historical results are unavailable, we can relax the sparse constraints of the matrixes $\tilde{\mathbf{a}}_s^v$ and $\tilde{\mathbf{a}}_r^k$ to get coarse results, based on which the ranges of delay parameters. Therefore, the proposed solution strategy can efficiently avoid the combinational explosion problem and is practical for real-world applications.

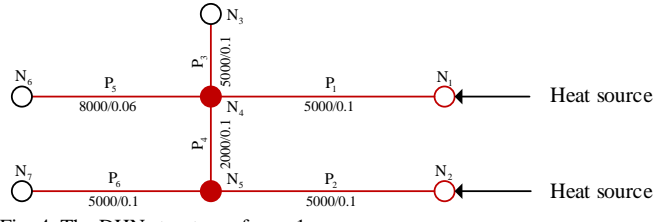


Fig. 4 The DHN structure of case 1.

TABLE I
SETTINGS OF TESTS

Test No.	1	2	3	4	5 ^a	6 ^b
Standard deviation σ	0	1.0%	1.0%	1.0%	1.0%	1.0%
Proportion of outliers	0	0	10%	20%	10%	10%

Note: ^arelaxing normalization constraints; ^brelaxing sparsity constraints.

IV. NUMERICAL TEST

Two DHNs of different scales are simulated to verify the proposed method's effectiveness. Case I is based on a 7-node DHN to verify the accuracy of the AGM. Case II uses a real-world 42-node DHN located in Beijing, China. The operation data of Case I are obtained using the node method-based simulation. The operation data of Case II is from real-world measurement. The simulation platform is a laptop computer with an Intel i7 CPU and 16GB RAM. The programming environment is Matlab R2022a and Yalmip. Gurobi 10.0.1 is used to solve the (mixed-integer) quadratic programming problem.

Three metrics were used to assess the goodness-of-fit of the good, including the root mean square error (RMSE), the mean absolute percentage error (MAPE), and the coefficient of determination (R^2), as follows.

$$\text{RMSE} = \sqrt{\frac{1}{1+T} \sum_{t=0}^T (\tilde{\tau}_t - \tau_t)^2},$$

$$\text{MAPE} = \frac{1}{1+T} \sum_{t=0}^T |(\tilde{\tau}_t - \tau_t) / \tau_t|,$$

$$R^2 = 1 - \frac{\sum_{t=0}^T (\tilde{\tau}_t - \tau_t)^2}{\sum_{t=0}^T \left(\tau_t - \frac{1}{1+T} \sum_{t=0}^T \tau_t \right)^2},$$

wherein T is the number of samples, $\tilde{\tau}_t$ is the temperature calculated by AGM, and τ_t is the operation data.

A. Case I: An Illustrative Network

The DHN in this case is shown in Fig. 4. The training and test data include 400 and 100 samples, respectively, with a resolution of 60 minutes. We perform several tests to verify the proposed method, the settings of which are given in Table I. Considering that the measurement error of the real-world DHN is usually below 1.0%, we add the Gaussian noises with 1.0% standard deviations to the exact data in Tests 2-6. In Tests 3-6, we add different proportions of outliers to data to investigate the robustness of the estimator. As mentioned in Section II, the theoretical values of the parameters in the AGM can be derived easily by (3a)-(4c). The model order in Tests 1-5 is set to 4 based on the theoretical results. Due to the page limitation, only the test results of the load node N_6 and the source node N_2 are analyzed in the following.

TABLE II
AGGREGATE PARAMETERS OF N_6 SOLVED BY HME IN CASE 1

Test No.	$\gamma_{agg}^{1,6}$	Coefficients of $\tau_{s,src}^{1,t-2-i}$ (i.e., $\tilde{a}_s^{1,6,i}$)					
		$i=-2$	$i=-1$	$i=0$	$i=1$	$i=2$	$i=3$
Theoretical	2	/ ^a	/	0.38	0.23	0.026	0
1	2	/	/	0.38	0.23	0.026	0 ^b
2	1	/	3.4e-4	0.38	0.22	0.023	/
3	1	/	3.7e-3	0.38	0.22	0.025	/
4	0	6.5e-3	3.7e-3	0.38	0.22	/	/
5	1	/	6.4e-3	0.37	0.22	0.022	/

Test No.	$\gamma_{agg}^{2,6}$	Coefficients of $\tau_{s,src}^{2,t-2-i}$ (i.e., $\tilde{a}_s^{2,6,i}$)						b_s^k
		$i=-1$	$i=0$	$i=1$	$i=2$	$i=3$	$i=4$	
Theoretical	2	/	1.4e-3	0.075	0.11	0.015	/	0.17
1	2	/	1.4e-3	0.075	0.11	0.015	/	0.17
2	2	/	6.9e-3	0.079	0.10	0.016	/	0.17
3	1	6.2e-3	8.2e-3	0.080	0.11	/	/	0.17
4	2	/	5.8e-3	0.079	0.11	0.019	/	0.17
5	1	3.4e-3	5.3e-3	0.078	0.11	/	/	0.094

Test No.	$\gamma_{agg}^{1,6}$	Coefficients of $\tau_{s,src}^{1,t-1-i}$ (i.e., $\tilde{a}_s^{1,6,i}$)					
		$i=0$	$i=1$	$i=2$	$i=3$	$i=4$	$i=5$
6	1	6.9e-4	0.38	0.22	0.023	5.0e-4	0 [*]

Test No.	$\gamma_{agg}^{2,6}$	Coefficients of $\tau_{s,src}^{2,t-2-i}$ (i.e., $\tilde{a}_s^{2,6,i}$)						b_s^k
		$i=0$	$i=1$	$i=2$	$i=3$	$i=4$	$i=5$	
6	2	5.5e-3	0.078	0.11	0.012	0 [*]	7.2e-3	0.17

^a"/" denotes the model does not include this parameter, i.e., the default is 0;^bThe parameter below 1e-4 is denoted as 0^{*}.

1) Accuracy of the AGM

The theoretical and estimated values of the parameters of the STM of N_6 (s) and the RTM of N_2 are given in Table II and Table III, respectively. Test 1 indicates that the estimated parameters are in complete agreement with the theoretical values under noise-free data, verifying the theoretical accuracy of AGM. Although for the RTM of N_2 , the value of $\gamma_{agg}^{2,7}$ in Test 1 is not correctly estimated, as shown in Table III, it does not affect the accuracy of the model parameters. The reason is that the theoretical values of the parameters $\tau_{r,l}^{7,t-1-i}$ are nonzeros only for $i=0,1,2$, so the parameters can be always precisely estimated when γ_{agg} takes any value of 0, 1, or 2. This also explains why the model parameters can be estimated accurately in other tests, although the delay parameters are not correctly estimated. Also, in Test 1, the values of $\tau_{s,src}^{1,t-2-i}$ ($i=3$) and $\tau_{r,l}^{7,t-1-i}$ ($i=-1$) are not strictly equal to the theoretical value 0. This comes from the numerical calculation-induced errors, whose impact is marginal and can be ignored.

Another interesting phenomenon is that for every node, the dominant values of the parameters $\tilde{a}_s^{k,v,i}$ (or $\tilde{a}_r^{k,v,i}$) are distributed in two adjacent positions, as shaded in blue in Table II and Table III. This proves the sparsity of the parameters \tilde{a}_s^v and \tilde{a}_r^k , verifying the rationality of the proposed sparsity-based enhancement strategy.

2) Robustness analysis

In Tests 3-6, the outliers of varying proportions are added to the node temperature. We use the salt-and-pepper noise to simulate outliers [27-29], a common form of pulse noise. The probability distribution of the added noise is as

TABLE III
AGGREGATE PARAMETERS OF N_2 SOLVED BY HME IN CASE 1

Test No.	$\gamma_{agg}^{2,3}$	Coefficients of $\tau_{r,l}^{3,t-2-i}$ (i.e., $\tilde{a}_r^{2,3,i}$)					
		$i=-1$	$i=0$	$i=1$	$i=2$	$i=3$	$i=4$
Theoretical	2	/ ^a	0 ^b	2.5e-3	0.046	0.057	/
1	2	/	0*	2.5e-3	0.046	0.057	/
2	2	/	0.012	0*	0.065	0.054	/
3	1	7.9e-3	0.017	0*	0.098	/	/
4	2	/	0.016	0*	0.071	0.054	/
5	1	1.6e-3	0.012	0*	0.090	/	/

Test No.	$\gamma_{agg}^{2,6}$	Coefficients of $\tau_{r,l}^{6,t-2-i}$ (i.e., $\tilde{a}_r^{2,6,i}$)					
		$i=-1$	$i=0$	$i=1$	$i=2$	$i=3$	$i=4$
Theoretical	2	/	6.8e-4	0.038	0.054	7.4e-3	/
1	2	/	6.8e-4	0.038	0.054	7.4e-3	/
2	2	/	0*	0.038	0.051	0*	/
3	1	0*	0*	0.040	0.050	/	/
4	2	/	0*	0.033	0.048	0*	/
5	1	0*	0*	0.041	0.045	/	/

Test No.	$\gamma_{agg}^{2,7}$	Coefficients of $\tau_{r,l}^{7,t-1-i}$ (i.e., $\tilde{a}_r^{2,7,i}$)					b_r^k
		$i=-1$	$i=0$	$i=1$	$i=2$	$i=3$	
Theoretical	1	/	8.6e-3	0.47	0.21	0	0.11
1	0	0*	8.6e-3	0.47	0.21	/	0.11
2	0	2.8e-3	9.8e-3	0.45	0.21	/	0.11
3	1	/	0.014	0.46	0.21	0*	0.11
4	2	/	/	0.46	0.21	0*	0.11
5	1	/	8.6e-3	0.45	0.21	0*	0.021

Test No.	$\gamma_{agg}^{2,3}$	Coefficients of $\tau_{r,l}^{3,t-2-i}$ (i.e., $\tilde{a}_r^{2,3,i}$)					
		$i=0$	$i=1$	$i=2$	$i=3$	$i=4$	$i=5$
6	2	5.2e-3	0*	0.068	0.051	0*	0*

Test No.	$\gamma_{agg}^{2,6}$	Coefficients of $\tau_{r,l}^{6,t-2-i}$ (i.e., $\tilde{a}_r^{2,6,i}$)					
		$i=0$	$i=1$	$i=2$	$i=3$	$i=4$	$i=5$
6	2	0*	0.042	0.048	1.8e-3	0*	0*

Test No.	$\gamma_{agg}^{2,7}$	Coefficients of $\tau_{r,l}^{7,t-2-i}$ (i.e., $\tilde{a}_r^{2,7,i}$)					b_r^k
		$i=0$	$i=1$	$i=2$	$i=3$	$i=4$	
6	2	0.012	0.45	0.20	0*	4.8e-3	1.8e-3

^a “/” denotes the model does not include this parameter, i.e., the default is 0;

^b The parameter below 1e-4 is denoted as 0*.

$$p(z) = \begin{cases} P_a & z = a \\ P_b & z = b \\ 1 - P_a - P_b & z = 1 \end{cases},$$

wherein, z is the ratio of the noise data added to the original data; P_a and P_b are the probability of outliers. In the simulations, a is set to 3 and b is set to 0.3; and we set $P_a = P_b$. The proportion of outliers P equals to $P_a + P_b$.

The results in Table II and Table III indicate that the parameters b_s^k and b_r^k can be always precisely estimated in Tests 3-4. The estimation errors of $\tilde{a}_s^{k,v,i}$ are also small. However, the parameter $\tilde{a}_r^{2,3,i}$ is not accurately estimated. One reason is that the values of $\tilde{a}_r^{k,v,i}$ for some v will be very small if the mass flow rate from the load node v to the source node k is small, i.e., the return temperature of this node $\tau_{r,l}^{v,t}$ contributes less to the that of the source node $\tau_{r,src}^{k,t}$. In this situation, the parameter $\tilde{a}_r^{k,v,i}$ is insensitive to the operation data and thus hard to be accurately estimated. Therefore, the results of Tests 3-4 indicate that the outliers could deteriorate the performance of the HME for insensitive parameters.

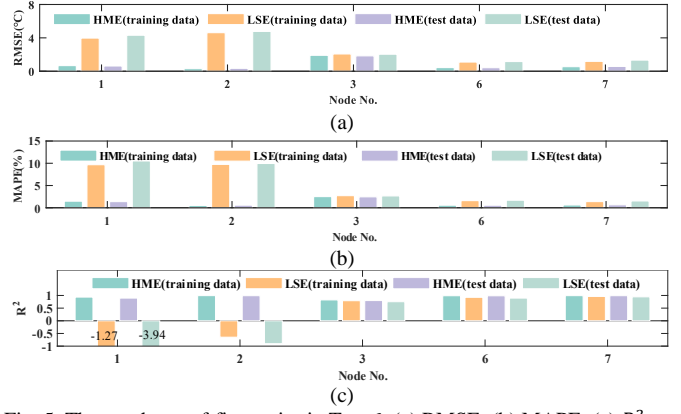


Fig. 5 The goodness-of-fit metrics in Test 6: (a) RMSE; (b) MAPE; (c) R^2 .

Fortunately, the error of the RTM caused by this situation is usually very small since the contribution of $\tau_{r,l}^{v,t}$ to $\tau_{r,src}^{k,t}$ is small. Specifically, for the return temperature of the source node N_2 , the load nodes N_3 , N_6 , and N_7 and the ambient temperature contribute about 10.5%, 10%, 68.8%, and 11%, respectively. The goodness-of-fit metrics of Test 6, as given in Fig. 5, will also provide solid proof. Fig. 5 shows that the proposed HME has excellent goodness-of-fit metrics for all the nodes.

As shown in Fig. 5, the proposed method has significantly improved the estimation accuracy compared to the traditional LSE. Especially, the values of R^2 of the LSE for the nodes N_1 and N_2 are negative, indicating that the model cannot capture data trends. In conclusion, the proposed HME for the AGM significantly improves the robustness to outliers.

3) Effect of physics-informed structural constraints

The effect of the physics-informed structural constraints can be revealed by comparing the results of Test 3 and Tests 5-6. The results of Test 5 indicate that the values of b_s^k and b_r^k cannot be accurately estimated after relaxing the normalization constraints, as shaded in grey in Table II and Table III.

The order of the model in Test 6 is set to 6 to make it more accurate, higher than Test 3. The results of Test 6 indicate that the model parameters can be estimated with reasonable accuracy after relaxing sparsity constraints, although the accuracy is sometimes lower than in Test 3. However, a potential risk of relaxing sparsity constraints is obtaining a physically unrealistic model, the most critical deficiency. For example, as shown in Table III, the nonzero locations of the parameters $\tilde{a}_r^{2,3,i}$ are not continuously distributed from $i=-1$ to 4, violating the heat transmission law of DHN. Besides, it should be noted that Test 6 also needs to estimate the range of the transmission delay of nodes before the parameter estimation to ensure the dimensions of the matrix \tilde{a}_s^v and \tilde{a}_r^k finite. Therefore, relaxing the sparsity constraints usually requires a higher-order model to ensure accuracy, which is another shortcoming.

On the other hand, as stated in **Remark 5**, Test 6 can provide an initial estimation for the parameters, which can then be used to provide a fine estimation for the delay parameters. This will efficiently improve the computational performance of the proposed model since the set of delay parameters is narrowed, especially when the historical information on the delay parameters is unavailable.

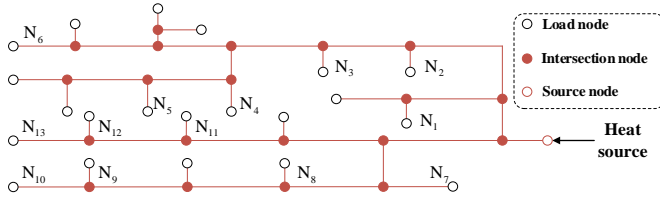
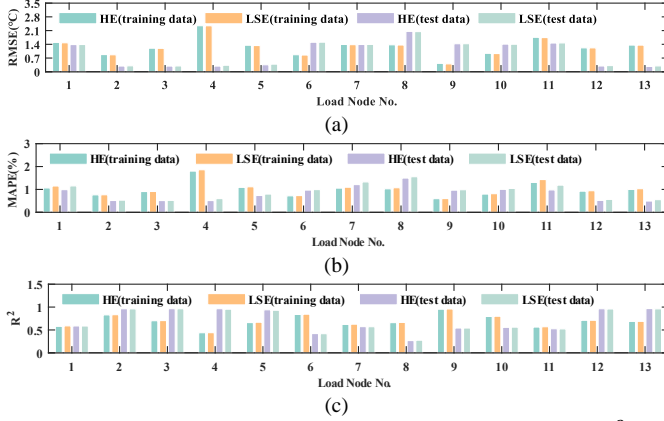


Fig. 9 Topology of DHN in case 2.

Fig. 10 Goodness-of-fit metrics of Case II: (a) RMSE; (b) MAPE; (c) R^2 .

B. Case II: A Real-World Network

The structure of DHN in Case II is given in Fig. 9. The training data and test data include 200 and 100 samples, respectively, with a resolution of 30 minutes. Due to incomplete real-world operation data, only the AGMs of the partial supply network are tested, as labeled in Fig. 9. This is sufficient to prove the effectiveness of the AGM. To balance the computational cost and accuracy, we use the 3-horizon AGM.

The performance of the LSE and HME for the AGM are given in Fig. 10. The results indicate that both methods perform well while the HME is better than LSE for some nodes (e.g., N_6 - N_{11}). Overall, the superiority of the HME cannot be fully exploited in this case because of the small proportions of outliers in the measurement (about 1% of the total data). Therefore, for the AGM, the gain of the HME compared to the LSE depends on the measurement quality.

Besides, the goodness-of-fit metrics of the training data of some nodes are worse than those of the test data, e.g., N_3 - N_5 and N_{10} - N_{13} . The reason is that there are more outliers in the training data of these nodes. Note that although the outliers have been filtered by HME, they will still have a negative impact on the goodness-of-fit metrics. Furthermore, Fig. 6 gives the results of the AGM on both the training and test data. In summary, we can conclude that the AGM can accurately describe the input-output characteristics of DHN, the accuracy of which is enough for the operation and control requirements of energy systems.

More detailed simulation results are provided in [30].

C. Verification of AGM in Economic Dispatch

In this part, we investigate the performance of AGM in the economic dispatch (ED) problem of IES to verify its engineering application values. Two systems of different scales are investigated. For each system, two different subcases are

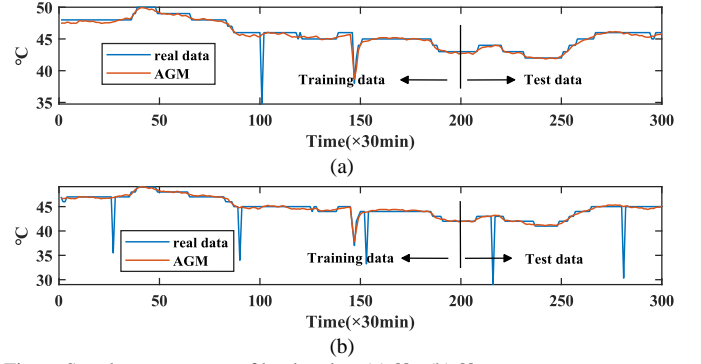
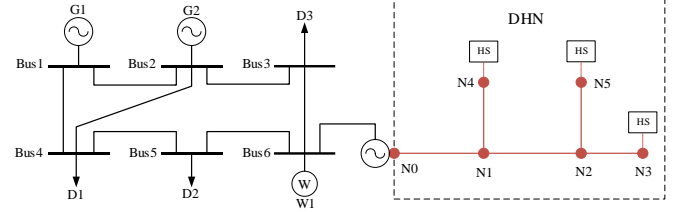
Fig. 6 Supply temperature of load nodes: (a) N_2 ; (b) N_8 .

Fig. 7 Structure of IES in the small-scale system.

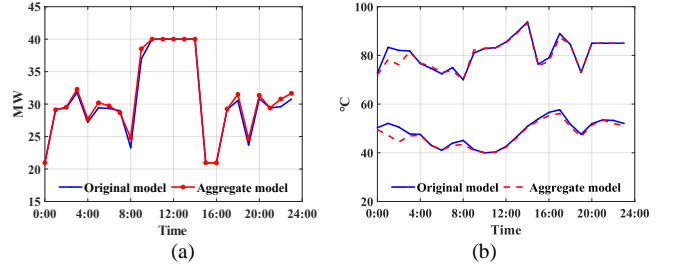


Fig. 8 (a) The thermal power output of CHP in different models; (b) Supply/return temperature of the source node in different models.

simulated, respectively, in which Subcase I is based on the node method model; and Subcase II is based on the AGM. In the simulations, the dispatch period is set to 24 hours, the time interval is set to 1 hour, and the time resolution of the DHN and the building is set to 60 min. The initial state of the building is set to 21°C, and the upper and lower limits of the indoor temperature are set to 24°C and 18°C, respectively.

1) Small-scale system

The structure of the IES in this case is given in Fig. 7. The system consists of a 6-bus power system and a 6-node DHN. The dispatch model is a quadratic programming problem. The order of the AGM is set to 4. The dispatch results are shown in Fig. 8. In the two subcases, the thermal power output of the CHP unit, namely the thermal power injected into the DHN, is almost the same. Also, the heat energy output of the generation units in the two subcases is nearly the same. The results in Fig. 8 (b) show that the deviations between the supply (and return) temperatures of the two subcases are marginal. The dispatch costs and solver time are given in Table IV. The results indicate that the differences between the AGM and the node method model in the ED problem can be fully ignored.

2) Large-scale system

The IES in this case consists of a modified Polish 2383-bus power system and 20 DHNs. The power system contains 20 CHP units. Each CHP unit provides heat for a separate DHN. The topology of the DHN is modified from the DHN in [7],

TABLE IV
RESULTS OF THE SMALL-SCALE SYSTEM

DHN model	Cost ($\times 10^3 \text{ ¥}$)	Solver time
Node method	102.3912	0.1239s
AGM	102.4989	0.0795s
Deviation	1.05‰	/

TABLE V
RESULTS OF THE LARGE-SCALE SYSTEM

DHN model	Cost ($\times 10^6 \text{ ¥}$)	Heat energy of CHP (MWh)	Solver time
Node method ^a	\	\	$\geq 12\text{h}$
AGM	48.0103	70902	9190
Node method ^b	47.5433	68959	42.69s
AGM ^b	47.6914	69853	13.93s
Deviation	3.1‰	1.5%	/

^a The solver fails to finish within 12 hours;

^b The binary variables denoting charging/discharging states are relaxed.

which contains 222 pipes and 223 nodes and provides heat for 112 heating exchange substations. The 20 DHNs have the same topology structure but different network parameters. Each DHN is equipped with a thermal storage tank at the source node. The dispatch model is a mixed-integer quadratic programming problem. The order of the AGM is set to 4. The simulation results, including the dispatch cost, output, and solver time, are given in Table V. The results show that the AGM model slightly increased the dispatch cost and the heat energy, but the amount is negligible. A potential reason is that the truncated AGM underestimates the supply/return temperature. It is worth mentioning that the solver time of the ED model based on the AGM is significantly reduced, revealing the significant computational advantages and the application potential of AGM, especially in large-scale systems.

In summary, the results demonstrate that the proposed AGM has good application prospects in the integrated energy optimization problem.

V. CONCLUSION

The traditional DHN model relying on detailed pipeline modeling faces identifiability issues under limited measurement in engineering. To address this problem, this paper develops an aggregate model for DHN that combines physical insights with data-driven techniques. The contributions of this work include the analytical expressions for the state relationship of source and load nodes, i.e., the AGM, a Huber M-estimator with physics-informed structural constraints for the parameter estimation of AGM, and an effective solution algorithm. Overall, our approach offers a promising solution for modeling DHN, overcoming identifiability challenges and providing a foundation for integrated energy optimization.

Our future research will focus on 1) integrating buildings' thermal inertia into the AGM and 2) exploring the model identification of DHN under the variable flow control strategy.

REFERENCES

- [1] X. Y. Chen *et al.*, "Integrated Energy Systems for Higher Wind Penetration in China: Formulation, Implementation, and Impacts," *IEEE Trans. Power Syst.*, vol. 33, no. 2, pp. 1309-1319, Mar, 2018.
- [2] J. W. Yang *et al.*, "A Cost-Sharing Approach for Decentralized Electricity-Heat Operation With Renewables," *IEEE Trans. Sustainable Energy*, vol. 11, no. 3, pp. 1838-1847, Jul, 2020.
- [3] K. W. Hu *et al.*, "Comparative study of alkaline water electrolysis, proton exchange membrane water electrolysis and solid oxide electrolysis through multiphysics modeling," *Appl. Energy*, vol. 312, Apr 15, 2022.
- [4] Z. G. Li *et al.*, "Combined Heat and Power Dispatch Considering Pipeline Energy Storage of District Heating Network," *IEEE Trans. Sustainable Energy*, vol. 7, no. 1, pp. 12-22, Jan, 2016.
- [5] Z. G. Li *et al.*, "Transmission-Constrained Unit Commitment Considering Combined Electricity and District Heating Networks," *IEEE Trans. Sustainable Energy*, vol. 7, no. 2, pp. 480-492, Apr, 2016.
- [6] H. Wang *et al.*, "Improved thermal transient modeling with new 3-order numerical solution for a district heating network with consideration of the pipe wall's thermal inertia," *Energy*, vol. 160, pp. 171-183, Oct 1, 2018.
- [7] E. W. Gong *et al.*, "Optimal operation of novel hybrid district heating system driven by central and distributed variable speed pumps," *Energy Convers. Manage.*, vol. 196, pp. 211-226, Sep 15, 2019.
- [8] H. Madsen *et al.*, *Models and Methods for Optimization of District Heating Systems. Part II: Models and Control Methods*, Technical University of Denmark: Institut for Matematisk Statistik og Operationsanalyse, 1992.
- [9] V. D. Stevanovic *et al.*, "Prediction of thermal transients in district heating systems," *Energy Convers. Manage.*, vol. 50, no. 9, pp. 2167-2173, Sep, 2009.
- [10] A. Benonysson, "Dynamic Modelling and Operational Optimization of District Heating Systems," Laboratory of Heating and Air Conditioning, Technical University of Denmark, 1991.
- [11] H. Palsson, "Analysis of numerical methods for simulating temperature dynamics in district heating pipes," *Proceedings of the 6. International Symposium on District Heating and Cooling Simulation*, pp. 1-20, 1997.
- [12] A. Benonysson *et al.*, "Operational Optimization in a District-Heating System," *Energy Convers. Manage.*, vol. 36, no. 5, pp. 297-314, May, 1995.
- [13] I. Gabrieliutienė *et al.*, "Modelling temperature dynamics of a district heating system in Naestved, Denmark - A case study," *Energy Convers. Manage.*, vol. 48, no. 1, pp. 78-86, Jan, 2007.
- [14] I. Gabrieliutienė *et al.*, "Dynamic temperature simulation in district heating systems in Denmark regarding pronounced transient behaviour," *Journal of Civil Engineering and Management*, vol. 17, no. 1, pp. 79-87, 2011.
- [15] B. Bøhm *et al.*, "Equivalent Models for District Heating Systems," *Proceedings of the 7th International Symposium on District Heating and Cooling*, pp. 1-16, 1999.
- [16] H. V. Larsen *et al.*, "Aggregated dynamic simulation model of district heating networks," *Energy Convers. Manage.*, vol. 43, no. 8, pp. 995-1019, May, 2002.
- [17] B. Bøhm *et al.*, "Simple Models for Operational Optimisation," in 8th International Symposium on District Heating and Cooling, Trondheim, Norway, 2002.
- [18] H. V. Larsen *et al.*, "A comparison of aggregated models for simulation and operational optimisation of district heating networks," *Energy Convers. Manage.*, vol. 45, no. 7-8, pp. 1119-1139, May, 2004.
- [19] H. Zhao, *Analysis, modelling and operational optimization of district heating systems*, Denmark, 1995.
- [20] A. La Bella *et al.*, "Data-driven modelling and optimal management of district heating networks," *2021 AEIT International Annual Conference (AEIT)*, 2021, pp. 1-6.
- [21] L. Di Natale *et al.*, "Towards scalable physically consistent neural networks: An application to data-driven multi-zone thermal building models," *Appl. Energy*, vol. 340, 2023.
- [22] W. Y. Zheng *et al.*, "A Dynamic Equivalent Model for District Heating Networks: Formulation, Existence and Application in Distributed Electricity-Heat Operation," *IEEE Trans. Smart Grid*, vol. 12, no. 3, pp. 2685-2695, May, 2021.
- [23] S. H. Zhang *et al.*, "Dynamic Security Control in Heat and Electricity Integrated Energy System With an Equivalent Heating Network Model," *IEEE Trans. Smart Grid*, vol. 12, no. 6, pp. 4788-4798, Nov, 2021.
- [24] S. Lu *et al.*, "Thermal Inertial Aggregation Model for Integrated Energy Systems," *IEEE Trans. Power Syst.*, vol. 35, no. 3, pp. 2374-2387, May, 2020.
- [25] S. Lu *et al.*, "High-Resolution Modeling and Decentralized Dispatch of Heat and Electricity Integrated Energy System," *IEEE Trans. Sustainable Energy*, vol. 11, no. 3, pp. 1451-1463, Jul, 2020.
- [26] K. L. Zhou *et al.*, "Energy Internet: The business perspective," *Appl. Energy*, vol. 178, pp. 212-222, Sep 15, 2016.
- [27] X. Kang *et al.*, "A Novel Adaptive Switching Median filter for laser image based on local salt and pepper noise density," *2011 IEEE Power Engineering and Automation Conference*, 2011, pp. 38-41.
- [28] Y. Wan *et al.*, "A novel quadratic type variational method for efficient salt-and-pepper noise removal," *2010 IEEE International Conference on Multimedia and Expo*, 2010, pp. 1055-1060.
- [29] R. H. Chan *et al.*, "Salt-and-Pepper noise removal by median-type noise detectors and detail-preserving regularization," *IEEE Trans Image Process*, vol. 14, no. 10, pp. 1479-85, Oct, 2005.
- [30] "Supplementary Information," <https://github.com/Shuai-Lu/Aggregate-Model-of-DHN-A-Physically-Informed-Data-Driven-Approach>.